Inhomogeneous terminators on the exoplanet WASP-39 b

Espinoza, N.; Steinrueck, M.E.; Kirk, J.; MacDonald, R.J.; Savel, A.B.; Arnold, K.; ... ; Crouzet, N.M.

Article

Inhomogeneous terminators on the exoplanet WASP-39 b

https://doi.org/10.1038/s41586-024-07768-4

Received: 1 September 2023

Accepted: 1 July 2024

Published online: 15 July 2024

Open access

Check for updates

Néstor Espinoza[1,2]✉, Maria E. Steinrueck[3,4], James Kirk[5], Ryan J. MacDonald[6], Arjun B. Savel[7], Kenneth Arnold[7], Eliza M.-R. Kempton[7], Matthew M. Murphy[8], Ludmila Carone[9], Maria Zamyatina[10], David A. Lewis[9,11], Dominic Samra[9], Sven Kiefer[9,12,13,14], Emily Rauscher[6], Duncan Christie[3], Nathan Mayne[10], Christiane Helling[9,11], Zafar Rustamkulov[2], Vivien Parmentier[15], Erin M. May[16], Aarynn L. Carter[17], Xi Zhang[18], Mercedes López-Morales[19], Natalie Allen[2], Jasmina Blecic[20,21], Leen Decin[12], Luigi Mancini[3,22,23], Karan Molaverdikhani[24,25], Benjamin V. Rackham[26,27], Enric Palle[28], Shang-Min Tsai[29], Eva-Maria Ahrer[30], Jacob L. Bean[4], Ian J. M. Crossfield[31], David Haegele[3], Eric Hébrard[10], Laura Kreidberg[3], Diana Powell[4], Aaron D. Schneider[12,32], Luis Welbanks[33], Peter Wheatley[30], Rafael Brahm[34,35,36] & Nicolas Crouzet[37]

Transmission spectroscopy has been a workhorse technique used over the past two decades to constrain the physical and chemical properties of exoplanet atmospheres[1–5]. One of its classical key assumptions is that the portion of the atmosphere it probes—the terminator region—is homogeneous. Several works from the past decade, however, have put this into question for highly irradiated, hot ($T_{eq} \gtrsim 1{,}000$ K) gas giant exoplanets, both empirically[6–10] and through three-dimensional modelling[11–17]. While models have predicted clear differences between the evening (day-to-night) and morning (night-to-day) terminators, direct morning and evening transmission spectra in a wide wavelength range have not been reported for an exoplanet so far. Under the assumption of precise and accurate orbital parameters for the exoplanet WASP-39 b, here we report the detection of inhomogeneous terminators on WASP-39 b, which has allowed us to retrieve its morning and evening transmission spectra in the near-infrared (2–5 μm) using the James Webb Space Telescope. We have observed larger transit depths in the evening, which are, on average, 405 ± 88 ppm larger than the morning ones, and also have qualitatively larger features than the morning spectrum. The spectra are best explained by models in which the evening terminator is hotter than the morning terminator by 177^{+65}_{-57} K, with both terminators having C/O ratios consistent with solar. General circulation models predict temperature differences broadly consistent with the above value and point towards a cloudy morning terminator and a clearer evening terminator.

Our study was performed using observations of the exoplanet WASP-39 b from the James Webb Space Telescope (JWST) Transiting Exoplanet Community Director's Discretionary Early Release Science (ERS) programme (ERS-1366; Principal Investigators: N. M. Batalha, J. L. Bean and K. B. Stevenson)[18,19]. This highly irradiated gas giant exoplanet has a mass of $0.28M_{Jup}$, a radius of $1.27R_{Jup}$ and an equilibrium temperature of 1,100 K. The ERS observations consisted of four transit events, observed using four different JWST instruments. Combined, these revealed prominent atomic and molecular absorption features in the terminator region, including K, H_2O, CO_2, CO and even SO_2, the latter identified as a photochemical product[10,20–23]. Our analysis was performed, in particular, on the near-infrared spectrograph (NIRSpec)/PRISM-mode observations of WASP-39 b[10] because this dataset has the widest wavelength coverage while simultaneously presenting minimal instrumental systematics[24]. This dataset consists of an 8.23 h observation centred around the 10 July 2022 transit of WASP-39 b.

The JWST data were reduced using the FIREFLy pipeline[10], as described in ref. 24. Reference 24 also demonstrated that the majority of wavelengths less than 2 μm suffer from detector saturation, and are not in agreement with measurements performed using the near-infrared imaging and slitless spectrograph (NIRISS) single-object slitless spectroscopy (SOSS) instrument across a similar wavelength range[21]. Because a reliable determination of the transit depth less than 2 μm cannot be obtained using the NIRSpec/PRISM observations, we opted to use only the 2–5 μm data in our present analysis. We fit each individual wavelength-dependent light curve at the pixel-level resolution element of the instrument, using a simple linear term in time as our systematics model, following the work of ref. 10.

The transit light-curve analysis was performed by means of three different methodologies, all of which entailed different assumptions yet provided consistent results (Methods). We report on the results obtained using the catwoman framework[25,26], which is arguably the

A list of affiliations appears at the end of the paper.

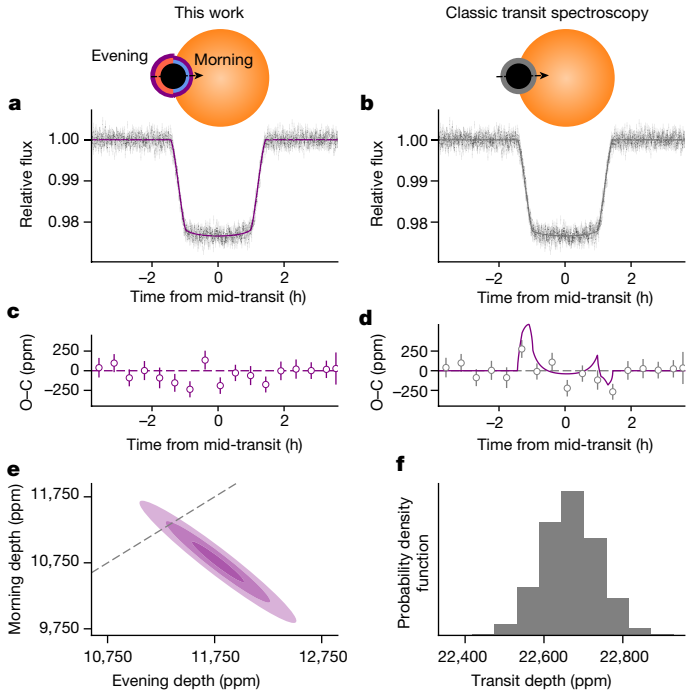

Fig. 1 | Light-curve modelling and extraction of morning and evening depths. **a**,**b**, Transit light-curve modelling of the 10 July 2022 transit at 4.38 μm (in the middle of the CO_2 spectral feature in the transmission spectrum) of WASP-39 b (grey datapoints) using both the catwoman framework (**a**, purple model) and the classic circular occulter model via batman (**b**, grey model). **c**,**d**, Residuals of the best-fit model for the catwoman (**c**) and batman (**d**) methodologies. The batman residuals (**d**) show, in turn, the difference between the catwoman and batman light-curve models (purple line), showcasing the catwoman model's small (approximately a few hundred parts per million) light-curve asymmetries. Note that the residuals are of comparable magnitude. While it is difficult to conclude the effect is present in each individual light curve, the effect is detectable once all the wavelength-dependent light curves have been analysed (see Fig. 2 and text for details). **e**,**f**, Inferences enabled from the catwoman (**e**) and batman (**f**) methodologies. The catwoman methodology (**e**) allows the extraction of morning/evening transit depths (purple ellipses representing the 1, 2 and 3σ posterior contours; dashed grey line indicating equal morning and evening depths), whereas the circular occulter methodology (**f**) only allows the extraction of a single total transit depth from the light curve. All error bars represent 1-standard deviation.

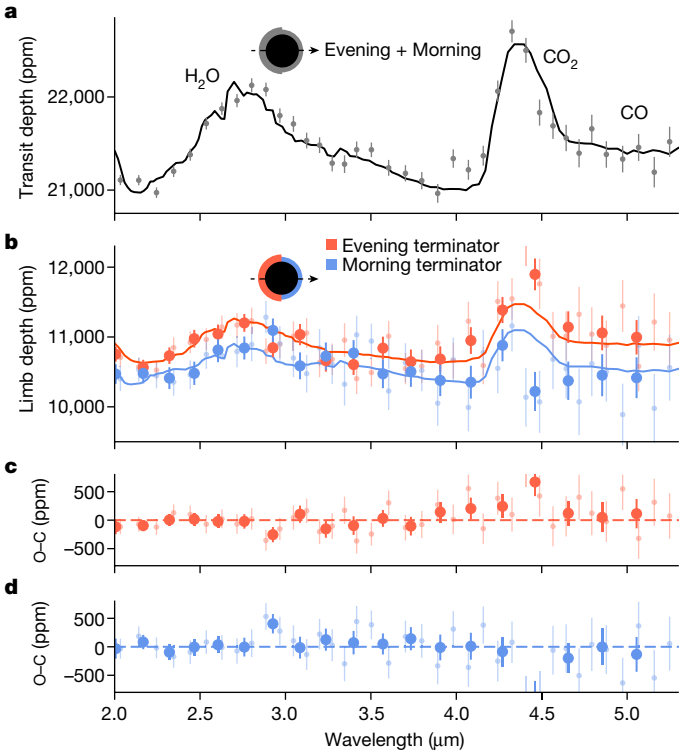

Fig. 2 | The morning and evening spectra of WASP-39 b from JWST NIRSpec/PRISM observations. **a**,**b**, The total transit depth, from adding the morning and evening spectra (**a**), along with the individual morning (blue points) and evening (red points) spectra of WASP-39 b, as derived from our light-curve modelling (**b**). The large points are datapoints at a resolution (R) of 30, shown for illustration, the smaller points are at $R = 100$. The best-fit, chemically consistent models (solid black line in **a**, solid red and blue lines in **b**; fitted to the $R = 100$ spectra) are consistent with a hotter evening terminator (see text for details). **c**,**d**, Residuals from the best-fit model (red points for the evening (**c**), blue points for the morning (**d**)), the dashed line marks 0. All error bars represent 1-standard deviation.

most conservative of the approaches because it allows fitting for morning and evening terminators simultaneously in a single fit. The framework models the terminator as two semicircles of independent radii, thus allowing us to separately retrieve the sizes of both morning and evening limbs as a function of the wavelength from the transit light curves themselves. An example light-curve fit at 4.38 μm, using this methodology and the classic circular occulter method—here, modelled using the batman library[27]—is presented in Fig. 1. More details on the data analysis are given in the Methods.

The resulting morning and evening terminator spectra inferred from our catwoman light-curve fits are presented in Fig. 2b. We computed an average difference between the evening and morning spectra of 405 ± 88 ppm, finding this difference to be inconsistent with 0 at more than 4.6σ—that is, the spectra showed statistically distinct features in the morning and evening terminators. Qualitatively, both the morning and evening spectra showcase transit depth increases at around the H_2O (2.84 μm) and CO_2 (4.38 μm) features, with the morning spectra being consistent with somewhat flatter spectra—a behaviour we observed with all our light-curve fitting methodologies. This detection of evening-to-morning spectral differences was, in turn, robust at the 3σ level, even when accounting for the current best uncertainties on the orbital parameters of WASP-39 b. This result does, however, depend on the accuracy and precision of those parameters up to a factor of a few of their current state-of-the-art error bars, which highlights the importance of the accurate and precise determination of exoplanetary orbital parameters when attempting to perform morning-to-evening spectroscopy, as we do in our work (Methods).

Next, we performed forward modelling and atmospheric retrievals to explore the physical mechanism behind the difference in the observed morning and evening spectra. In particular, we used the ATMO forward-model grid[28] and the chemically consistent CHIMERA retrieval framework[29], with modifications that allowed them to perform morning and evening inference simultaneously and account for the covariance between these limb depths[26]. We thus fitted the morning and evening spectra of WASP-39 b simultaneously to constrain their individual temperatures, C/O ratios and cloud properties (Methods). The best-fit solutions from both of those frameworks are qualitatively similar; in Fig. 2, we show the CHIMERA median model as solid blue and red lines for the morning and evening, respectively. Both modelling frameworks returned similar constraints on the morning and evening temperatures and C/O ratios. Our CHIMERA retrievals converge to a $C/O_{evening} = 0.58^{+0.13}_{-0.16}$ and $C/O_{morning} = 0.57^{+0.17}_{-0.23}$, which are consistent with each other. These are, in turn, consistent with the ratios derived from the transmission spectroscopy analysis reported by the ERS team from the NIRSpec/PRISM observations[10]—that is, C/O ≈ 0.3–0.5. Our derived metallicity (assumed to be common for both limbs) is also consistent with the approximately 10× solar metallicity reported in

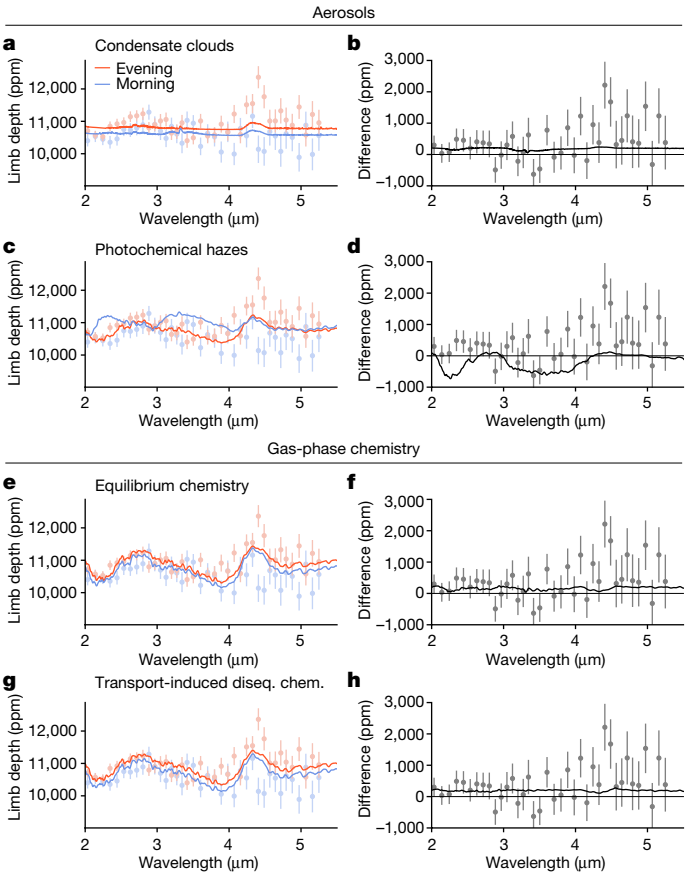

Fig. 3 | Comparison of morning and evening spectra using GCMs. **a**–**h**, Comparison between the predictions from GCMs and the observed transit depths for the morning and evening terminators, as derived with catwoman. The left-hand column shows the spectra (**a**, **c**, **e** and **g**) and the right-hand column shows the difference between the morning and evening terminator (**b**, **d**, **f** and **h**). A vertical offset of −600 ppm was applied to the spectra in **c**, **e** and **g** to facilitate comparison with the observed spectra. **a**,**b**, Condensate cloud model together with the equilibrium chemistry taking into account elemental depletion by clouds compared against the morning (blue) and evening (red) spectra (**a**), and against the difference between the spectra (**b**, in black); the grey line indicates zero difference. This model qualitatively provides the best match to the morning terminator spectrum. **c**,**d**, Photochemical haze model based on the SPARC/MITgcm, with equilibrium chemistry gas-phase abundances. **e**,**f**, Clear-atmosphere equilibrium chemistry model. **g**,**h**, Clear-atmosphere model, including transport-induced disequilibrium chemistry (diseq. chem.). The clear-atmosphere models provide the best match to the evening terminator spectrum. All error bars represent 1-standard deviation.

that work. Interestingly, the CHIMERA retrievals support a significantly hotter, 1068^{+43}_{-55} K, evening than the morning retrieved temperature of 889^{+54}_{-65} K, the difference being 177^{+65}_{-57} K—significant at more than a 3σ level. This result qualitatively follows predictions from three-dimensional (3D) general circulation models (GCMs), from which hotter evening limbs arise due to superrotating equatorial jets on highly irradiated exoplanets, such as WASP-39 b[14,15,23,30,31]. In addition, while the retrieval suggests a relatively constrained cloud-top location in the evening limb at about 1–10 mbar, the cloud-top location in the morning limb is relatively unconstrained, allowing multiple possible configurations, given this data. This is probably a consequence of the relatively flatter morning spectrum, combined with the relatively large uncertainties on our NIRSpec/PRISM limb spectra, allowing for a wide range of possibilities for the morning cloud properties. While this suggests that most of the variations observed in the NIRSpec/PRISM morning and evening limb spectra could be attributed to temperature differences between the morning and evening limbs, the treatment of clouds as grey opacity sources in the frameworks used to perform our inferences might be preventing us from further constraining the cloud properties in the morning and evening limbs of WASP-39 b.

To explore the possibilities enabled by aerosols and chemical processes, we compared the observations to predictions from GCMs, which are hydrodynamics models that simulate the 3D wind and temperature structure in planetary atmospheres, self-consistently predicting differences between the evening and morning terminator. A range of processes influence terminator differences in the spectra, including temperature differences driven by atmospheric circulation, condensate clouds, photochemical hazes and the transport-induced disequilibrium chemistry of gaseous species (Fig. 3). No single GCM is currently able to self-consistently simulate all of these processes simultaneously. We thus explored multiple different models[32–35].

While the gas-phase chemistry results (Unified Model) reproduced the shape of the spectral features well at the evening terminator, the condensate cloud model (ExpeRT/MITgcm) performed qualitatively better at reproducing the reduced feature amplitude at the morning terminator, especially the suppressed CO_2 feature at 4.3 μm. The photochemical haze model predicted large methane (CH_4) features at the morning limb and a larger morning limb in the CH_4 bands (centred at 2.3 and 3.3 μm), in conflict with the observations. This was driven by colder temperatures at low pressures in this GCM (Substellar and Planetary Atmospheric Radiation and Circulation (SPARC)/MITgcm) combined with the equilibrium chemistry. Photochemical hazes themselves have a smaller effect on limb differences. The condensate cloud model is the only one that predicted the largest limb difference to be in the centre of the CO_2 feature (even though the difference is substantially smaller than observed). This finding is in line with another recently published cloud-microphysics study[36]. A comparison with cloud-free spectra from the same GCM as our condensate cloud model (not shown) revealed that the limb difference in the centre of the 4.3 μm CO_2 feature is determined by the temperature difference, but, at other wavelengths, is dominated by clouds. We thus suggest, as a tentative explanation, a relatively cloud-free evening terminator and a cloudier morning terminator, in line with the inferences performed with the ATMO forward models and CHIMERA retrievals described above. Detailed follow-up studies, exploring a larger parameter space with cloud-formation models, will be needed to test this explanation.

Online content

Any methods, additional references, Nature Portfolio reporting summaries, source data, extended data, supplementary information, acknowledgements, peer review information; details of author contributions and competing interests; and statements of data and code availability are available at https://doi.org/10.1038/s41586-024-07768-4.

1. Seager, S. & Sasselov, D. D. Theoretical transmission spectra during extrasolar giant planet transits. *Astrophys. J.* **537**, 916–921 (2000).
2. Hubbard, W. B. et al. Theory of extrasolar giant planet transits. *Astrophys. J.* **560**, 413–419 (2001).
3. Burrows, A., Sudarsky, D. & Hubbard, W. B. A theory for the radius of the transiting giant planet HD 209458b. *Astrophys. J.* **594**, 545–551 (2003).
4. Fortney, J. J. The effect of condensates on the characterization of transiting planet atmospheres with transmission spectroscopy. *Mon. Not. R. Astron. Soc.* **364**, 649–653 (2005).
5. Kreidberg, L. in *Handbook of Exoplanets* (eds Deeg, H. J. & Belmonte, J. A.) 2083–2105 (Springer, 2018).
6. Louden, T. & Wheatley, P. J. Spatially resolved eastward winds and rotation of HD 189733b. *Astrophys. J. Lett.* **814**, L24 (2015).
7. Ehrenreich, D. et al. Nightside condensation of iron in an ultrahot giant exoplanet. *Nature* **580**, 597–601 (2020).
8. Prinoth, B. et al. Titanium oxide and chemical inhomogeneity in the atmosphere of the exoplanet WASP-189 b. *Nat. Astron.* **6**, 449–457 (2022).
9. Kesseli, A. Y., Snellen, I. A. G., Casasayas-Barris, N., Mollière, P. & Sánchez-López, A. An atomic spectral survey of WASP-76b: resolving chemical gradients and asymmetries. *Astron. J.* **163**, 107 (2022).

10. Rustamkulov, Z. et al. Early release science of the exoplanet WASP-39b with JWST NIRSpec PRISM. *Nature* **614**, 659–663 (2023).
11. Fortney, J. J. et al. Transmission spectra of three-dimensional hot Jupiter model atmospheres. *Astrophys. J.* **709**, 1396–1406 (2010).
12. Dobbs-Dixon, I., Agol, E. & Burrows, A. The impact of circumplantary jets on transit spectra and timing offsets for hot Jupiters. *Astrophys. J.* **751**, 87 (2012).
13. Line, M. R. & Parmentier, V. The influence of nonuniform cloud cover on transit transmission spectra. *Astrophys. J.* **820**, 78 (2016).
14. Kempton, E. M. R., Bean, J. L. & Parmentier, V. An observational diagnostic for distinguishing between clouds and haze in hot exoplanet atmospheres. *Astrophys. J. Lett.* **845**, L20 (2017).
15. Powell, D. et al. Transit signatures of inhomogeneous clouds on hot Jupiters: insights from microphysical cloud modeling. *Astrophys. J.* **887**, 170 (2019).
16. Helling, C. et al. Mineral cloud and hydrocarbon haze particles in the atmosphere of the hot Jupiter JWST target WASP-43b. *Astron. Astrophys.* **641**, A178 (2020).
17. MacDonald, R. J., Goyal, J. M. & Lewis, N. K. Why is it so cold in here? Explaining the cold temperatures retrieved from transmission spectra of exoplanet atmospheres. *Astrophys. J. Lett.* **893**, L43 (2020).
18. Stevenson, K. B. et al. Transiting exoplanet studies and community targets for JWST's Early Release Science Program. *Publ. Astron. Soc. Pac.* **128**, 094401 (2016).
19. Bean, J. L. et al. The transiting exoplanet community Early Release Science Program for JWST. *Publ. Astron. Soc. Pac.* **130**, 114402 (2018).
20. Alderson, L. et al. Early Release Science of the exoplanet WASP-39b with JWST NIRSpec G395H. *Nature* **614**, 664–669 (2023).
21. Feinstein, A. D. et al. Early Release Science of the exoplanet WASP-39b with JWST NIRISS. *Nature* **614**, 670–675 (2023).
22. Ahrer, E.-M. et al. Early Release Science of the exoplanet WASP-39b with JWST NIRCam. *Nature* **614**, 653–658 (2023).
23. Tsai, S.-M. et al. Photochemically produced SO_2 in the atmosphere of WASP-39b. *Nature* **617**, 483–487 (2023).
24. Carter, A. L. et al. A benchmark JWST near-infrared spectrum for the exoplanet WASP-39 b. *Nat. Astron.* https://doi.org/10.1038/s41550-024-02292-x (2024).
25. Jones, K. & Espinoza, N. catwoman: a transit modelling Python package for asymmetric light curves. *J. Open Source Softw.* **5**, 2382 (2020).
26. Espinoza, N. & Jones, K. Constraining mornings and evenings on distant worlds: a new semianalytical approach and prospects with transmission spectroscopy. *Astron. J.* **162**, 165 (2021).
27. Kreidberg, L. batman: basic transit model calculation in Python. *Publ. Astron. Soc. Pac.* **127**, 1161 (2015).
28. Goyal, J. M. et al. A library of ATMO forward model transmission spectra for hot Jupiter exoplanets. *Mon. Not. R. Astron. Soc.* **474**, 5158–5185 (2018).
29. Line, M. R. et al. A systematic retrieval analysis of secondary eclipse spectra. I. A comparison of atmospheric retrieval techniques. *Astrophys. J.* **775**, 137 (2013).
30. Kataria, T. et al. The atmospheric circulation of a nine-hot-Jupiter sample: probing circulation and chemistry over a wide phase space. *Astrophys. J.* **821**, 9 (2016).
31. Lee, E. K. H., Tsai, S.-M., Hammond, M. & Tan, X. A mini-chemical scheme with net reactions for 3D general circulation models. II. 3D thermochemical modelling of WASP-39b and HD 189733b. *Astron. Astrophys.* **672**, A110 (2023).
32. Carone, L., Lewis, D. A., Samra, D., Schneider, A. D. & Helling, C. WASP-39b: exo-Saturn with patchy cloud composition, moderate metallicity, and underdepleted S/O. Preprint at https://arxiv.org/abs/2301.08492 (2023).
33. Helling, C. et al. Exoplanet weather and climate regimes with clouds and thermal ionospheres. A model grid study in support of large-scale observational campaigns. *Astron. Astrophys.* **671**, A122 (2023).
34. Zamyatina, M. et al. Observability of signatures of transport-induced chemistry in clear atmospheres of hot gas giant exoplanets. *Mon. Not. R. Astron. Soc.* **519**, 3129–3153 (2023).
35. Steinrueck, M. E. et al. 3D simulations of photochemical hazes in the atmosphere of hot Jupiter HD 189733b. *Mon. Not. R. Astron. Soc.* **504**, 2783–2799 (2021).
36. Arfaux, A. & Lavvas, P. Coupling haze and cloud microphysics in WASP-39b's atmosphere based on JWST observations. *Mon. Not. R. Astron. Soc.* **530**, 482–500 (2024).

[1]Space Telescope Science Institute, Baltimore, MD, USA. [2]Department of Physics & Astronomy, Johns Hopkins University, Baltimore, MD, USA. [3]Max Planck Institute for Astronomy (MPIA), Heidelberg, Germany. [4]Department of Astronomy & Astrophysics, University of Chicago, Chicago, IL, USA. [5]Department of Physics, Imperial College London, London, UK. [6]Department of Astronomy, University of Michigan, Ann Arbor, MI, USA. [7]Department of Astronomy, University of Maryland, College Park, MD, USA. [8]Department of Astronomy and Steward Observatory, University of Arizona, Tucson, AZ, USA. [9]Space Research Institute, Austrian Academy of Sciences, Graz, Austria. [10]Department of Physics and Astronomy, Faculty of Environment, Science and Economy, University of Exeter, Exeter, UK. [11]Institute for Theoretical Physics and Computational Physics, Graz University of Technology, Graz, Austria. [12]Institute of Astronomy, KU Leuven, Leuven, Belgium. [13]Centre for Exoplanet Science, University of St Andrews, St Andrews, UK. [14]Fakultät für Mathematik, Physik und Geodäsie, TU Graz, Graz, Austria. [15]Observatoire de la Côte d'Azur, Université Côte d'Azur, CNRS, Nice, France. [16]Johns Hopkins APL, Laurel, MD, USA. [17]Department of Astronomy & Astrophysics, University of California, Santa Cruz, Santa Cruz, CA, USA. [18]Department of Earth and Planetary Sciences, University of California, Santa Cruz, Santa Cruz, CA, USA. [19]Center for Astrophysics, Harvard & Smithsonian, Cambridge, MA, USA. [20]Department of Physics, New York University Abu Dhabi, Abu Dhabi, UAE. [21]Center for Astro, Particle, and Planetary Physics (CAP3), New York University Abu Dhabi, Abu Dhabi, UAE. [22]Department of Physics, University of Rome "Tor Vergata", Rome, Italy. [23]INAF – Turin Astrophysical Observatory, Pino Torinese, Italy. [24]University Observatory Munich, Ludwig Maximilian University, Munich, Germany. [25]Exzellenzcluster Origins, Garching, Germany. [26]Department of Earth, Atmospheric and Planetary Sciences, Massachusetts Institute of Technology, Cambridge, MA, USA. [27]Kavli Institute for Astrophysics and Space Research, Massachusetts Institute of Technology, Cambridge, MA, USA. [28]Instituto de Astrofísica de Canarias (IAC), Tenerife, Spain. [29]Department of Earth Sciences, University of California, Riverside, Riverside, CA, USA. [30]Centre for Exoplanets and Habitability, University of Warwick, Coventry, UK. [31]Department of Physics & Astronomy, University of Kansas, Lawrence, KS, USA. [32]Centre for ExoLife Sciences, Niels Bohr Institute, Copenhagen, Denmark. [33]School of Earth and Space Exploration, Arizona State University, Tempe, AZ, USA. [34]Facultad de Ingeniería y Ciencias, Universidad Adolfo Ibáñez, Santiago, Chile. [35]Millennium Institute for Astrophysics, Santiago, Chile. [36]Data Observatory Foundation, Santiago, Chile. [37]Leiden Observatory, Leiden University, Leiden, The Netherlands. ✉e-mail: nespinoza@stsci.edu

Methods

Dataset

In this work, we use the JWST NIRSpec PRISM dataset, obtained for WASP-39 b as part of the JWST Transiting Exoplanet Community Director's Discretionary ERS programme[18,19] (ERS-1366; Principal Investigators: N. M. Batalha, J. L. Bean, K. B. Stevenson), which has already been introduced in ref. 10. We selected this dataset for the morning and evening exploration of WASP-39 b because, among the four ERS datasets, it has the widest wavelength coverage and presented relatively minor challenges in the light-curve data analysis, which is how we obtained constraints on the morning and evening of the exoplanet in this work.

Data analysis

We used the FIREFLy pipeline's reduction of the dataset, as presented in refs. 10,37 and subsequently used in ref. 24. To summarize, the pipeline performs initial calibrations using the package jwst, adding in group-stage 1/*f* noise destriping before the ramp-fitting stage. It then scrubs the time series of bad pixels and cosmic rays, and shift-stabilizes each integration to correct for millipixel-level correlated jitter of the spectral trace. Following the authors of ref. 24, who delved deeply into the deleterious effects of saturation, we elected to use only the unsaturated 2.0–5.0 μm region of the spectrum due to its weak systematic noise and reproducible transmission spectrum. The approximately 0.7–2.0 μm region showed significant deviations relative to the unsaturated NIRISS-SOSS spectrum[21], increasing in magnitude towards the saturation centre at 1.3 μm. The region also suffered from a significantly lower signal-to-noise ratio because fewer groups are available for use there. We omitted this region to avoid the possibility of drawing spurious conclusions about the planet's nature. We noted that WASP-39 b's 2.0–5.0 μm spectrum has relatively larger feature amplitudes, spanning more chemical species, than the NIR region. The PRISM spectrophotometry is well-fit by a linear trend varying in wavelength, and displays no other significant systematic noise.

Transit light-curve analysis

Physical and orbital parameters of the system. The physical and orbital parameters of WASP-39 b used in this work are the ones reported in ref. 24. These were fixed in our wavelength-dependent light-curve fits. In particular, we fixed the period to $P = 4.0552842$ days, the scaled-to-stellar-radius semi-major axis to $a/R_* = 11.390$ and the impact parameter to $b = 0.4498$, and set the mid-transit time for NIRSpec/PRISM to $T_0 = 2{,}459{,}771.335647$ days.

Wavelength-dependent light-curve analysis. To explore the evidence for morning and evening signatures on the wavelength-dependent NIRSpec/PRISM light curves, we performed analyses following three different approaches:

1. Catwoman light-curve fits. In this approach, we performed light-curve fits to the wavelength-dependent light curves using the catwoman framework introduced in refs. 25,26. This framework models the transiting object passing in front of the star as two stacked semicircles, each one representing the effective transit depth from the morning and evening terminators of WASP-39 b. We performed two sets of fits using this approach, led by co-authors M.M. (MM) and N.E. (NE), respectively, both of which set the rotation angle of the limbs to 90°. The NE catwoman fits were performed using limb-darkening coefficients taken from the limb-darkening[38] package as priors, using ATLAS models with the same stellar parameters as WASP-39, and passing those through the Synthetic-Photometry/Atmosphere-Model (SPAM) algorithm of ref. 39 to obtain the final estimates for the limb-darkening coefficients. The MM fits fixed the limb-darkening coefficients to those obtained from the ExoCTK[40] library also obtained from ATLAS models with the same stellar parameters as WASP-39. Both light-curve fits used a quadratic limb-darkening law. The NE fits used the limb-darkening parametrization in ref. 41, with a prior that followed a truncated normal centred around theoretical transformed coefficients (q_1, q_2), and with limits set at between 0 and 1 for each. The standard deviation of that prior distribution was set to 0.1 for both transformed coefficients, based on the findings of ref. 42, who found 0.1 to be the maximum offset between quadratic and empirical limb-darkening coefficients when comparing theoretical coefficients to those obtained via precise Transiting Exoplanet Survey Satellite photometry. Both fits also included a slope in time as a free parameter for modelling the visit-long slope seen in the NIRSpec/PRISM data in ref. 10, along with a baseline flux offset. The NE fits include, in addition, a jitter term added in quadrature to the NIRSpec/PRISM light-curve error bars. In total, the MM fits had four free parameters (two semicircle radii, slope and baseline flux offset) for each wavelength-dependent light curve, whereas the NE fits had seven free parameters (the same as MM plus two limb-darkening coefficients and a jitter term).
2. Ingress/egress (Tiberius) light-curve fits. In this approach, we performed transit light-curve fits to the wavelength-dependent light curves using the batman[27] framework via the Tiberius library[43,44], but fitting the half-ingress (where contributions mainly from the morning limb are expected) and half-egress (where contributions mainly from the evening limb are expected) independently. To find the contact points of the transit event, a transit light curve was generated using the orbital parameters described above, and limb-darkening was set to zero to find the discontinuity points in the light-curve-marking contact points—1 (start of ingress), 2 (end of ingress), 3 (beginning of egress) and 4 (end of egress). With this, the half-ingress (contact point 1.5—mean of contact 1 and 2) and half-egress (contact point 3.5—mean of contact 3 and 4) contact points were derived. The half-ingress (all datapoints before contact point 1.5 and after contact point 4) and half-egress (all datapoints after contact point 3.5 and before contact point 1) light curves were then fit as follows. First, the full light curve is fit for each wavelength bin, with a model that fits for a slope and baseline flux offset, the planet-to-star radius ratio and the linear term of a quadratic limb-darkening law, with the quadratic term fixed to limb-darkening coefficients obtained from 3D models in the Exo-TiC library[45]. Then, the half-ingress and half-egress light curves are fit by leaving all parameters fixed to the best-fit parameters obtained from the full transit fit, with the only free parameter being the planet-to-star radius ratios. These define the morning and evening transit depth, respectively, using this methodology.
3. Wavelength-dependent mid-transit time. The transit-time spectrum is sensitive to 0th-order wavelength-dependent opacity-centroid shifts along the planet's orbit, imparted by spatial inhomogeneity in the composition and temperature of its terminator[12,15,26,46]. A hotter, more extended trailing terminator casts a positive deflection in the relative transit time ($\Delta T_0 > 0$), with the planet appearing to transit slightly later due to the subtle trailing-limb inflation of its $\tau = 1$ surface. A colder leading terminator spectrum, or one with feature-muting grey clouds, would likewise cast a monochromatic positive deflection on the transit-time spectrum. The effect amplitude scales inversely with the planet's orbital velocity and impact parameter, and the difference in each terminator's mean transit-cord altitude. The time spectrum shown in Extended Data Fig. 1c is the result of a Levenburg–Marquardt least-squares fit to the spectrophotometry, with bins wider than those used in ref. 10. At each wavelength channel, we fixed WASP-39 b's orbital parameters to those of ref. 24, while fitting for its limb-darkening coefficients, transit depth and transit centre time using batman[27]. We found that the time signature is robust against the selection of fitted and fixed parameters, resulting in less than or equal to 1σ differences. Statistically significant greater than or equal to 3σ positive deflections were detected with wavelengths corresponding to the spectral features of H_2O (roughly 2–3.5 μm), H_2S (roughly 3.78 μm), SO_2 (roughly 4.06 μm) and CO_2 (roughly 4.2–4.5 μm).

The results from the methodologies described above are presented in Extended Data Fig. 1. Both catwoman (NE, MM) and the half-ingress and half-egress approaches seem to be consistent with each other within the error bars, and in judging the overall structure of the resulting morning and evening spectra. In general, it appears the morning spectral features of H_2O and CO_2 are damped in comparison with the same features observed in the evening—a picture that is consistent with the analysis performed on the wavelength-dependent transit times, where the largest offsets are observed for the H_2O and CO_2 features, although the latter molecule is seen at lower significance.

However, the significance of the dampening between spectral features in the morning and evening was less clear for the NE light-curve analysis. This approach produces the largest errors on the morning and evening spectra because this approach assumes some ignorance on the limb-darkening coefficients. As we show below, through light-curve experiments performed to study the robustness of our morning and evening spectra to assumptions on transit parameters, we deem this approach to be the most conservative, in terms of deriving differences between the morning and evening limbs, as very slight deviations from the true 'underlying' limb-darkening coefficients can give rise to false differences between morning and evening spectra, which can in turn be erroneously interpreted as an astrophysical effect in the exoplanet atmosphere. This is why we decided to perform inferences on the catwoman approach of NE to interpret the morning and evening spectra in the main text.

Robustness of morning and evening spectra to assumptions on transit parameters. Previous works that have studied the possibility of extracting morning and evening spectra directly from transit light curves have identified a number of possible degeneracies that might arise, and which could impact the derived spectra[15,26,46]. In particular, the degeneracy between the time-of-transit centre and limb asymmetries has been identified in previous works as the largest source preventing the performance of these detections in real data, with the use of precise wavelength-dependent transit light curves, such as the ones used in this work, being critical to lift it[15,46]. In addition, while limb-darkening has been shown to slightly decrease the detectability of limb asymmetries on simulated data[26], any biases induced by fixing those coefficients have, to our knowledge, not been studied in detail in the literature. Finally, eccentric orbits have been shown to also give rise to asymmetric transit light curves[47,48]. Using the wrong assumption about the eccentricity of the orbit could thus, in turn, give rise to biases on morning and evening spectra, which are extracted by measuring light-curve asymmetries. We performed experiments to study those three systematic error sources to quantify their impact on our reported morning and evening spectra.

Robustness against no limb asymmetries. To define a null baseline robustness check against the catwoman methodology used in this work, we simulated noisy transit light curves using batman, which had the same input transit parameters as the white-light light-curve parameters used in our fits (that is, the ones from ref. 24, the same noise properties as the real data (including the visit-long slope) and transit depths that varied as a function of the wavelength matching the transit spectrum presented in ref. 10. We then fitted those light curves with a catwoman model, using the same approach as the one described above for the NE catwoman light-curve fits. As expected, we found that the extracted morning and evening spectra were consistent with each other, producing a null difference between them. The results of those simulations are shown in Extended Data Fig. 3a.

Robustness against the time-of-transit centre. To check the robustness of our spectra against using a fixed time-of-transit centre (obtained from ref. 24), we performed the same simulations as the ones described in the previous section. However, we used a time-of-transit centre 3σ larger than the one reported in ref. 24, which amounted to a time offset of 3.4 s. We then fitted those light curves with a catwoman model, which used the time-of-transit centre as a fixed parameter without this offset. We found that such an offset in timing had no measurable impacts on our morning and evening transit spectra, with the difference between them being consistent with zero. The results of those simulations are shown in Extended Data Fig. 3b.

Robustness against limb-darkening coefficients. We performed a similar experiment to the one described in the previous section, but modified the input limb-darkening coefficients to be offset by 0.01 from the fixed values, which were obtained following the methodology described above for NE's catwoman transit light-curve fitting approach. We then fitted those light curves, but fixed the limb-darkening coefficients in our fit to the ones without those offsets. We found that these very small offsets on the limb-darkening coefficients had a measurable impact on the retrieved morning and evening spectra, giving rise to measurable morning and evening differences on the order of approximately 200–300 ppm when fixing those in the light-curve fitting procedure to the wrong values. The results from this simulation are presented in Extended Data Fig. 3c. The same experiment, but setting wide priors on these coefficients, as described in the NE catwoman light-curve fitting procedure above, allowed the input null difference between the evening and morning spectra (not shown) to be recovered. These experiments highlight that, while relative morning and evening spectral differences might be obtained by fixing the limb-darkening coefficients, even if they are slightly wrong, absolute spectral differences might not be robustly extracted in general. Even if aiming to obtain relative morning and evening spectral differences, in reality, limb-darkening offsets might be wavelength-dependent and thus might give rise to spurious signals and/or spectral features in the limb spectra. This was one of the main reasons we decided to present the results obtained from the NE catwoman light-curve fitting procedure in the main text—because it allows for limb-darkening coefficients to be significantly offset from the input theoretical model calculations. The limb-darkening coefficients retrieved from performing catwoman fits using the NE approach to our real NIRSpec/PRISM data are presented in Extended Data Fig. 4. Errors on the u_1 coefficients ranged from 0.02–0.04, while errors on the u_2 coefficients ranged from 0.03–0.06. Thus, offsets on the limb-darkening coefficients on the order of approximately 0.01, are indeed allowable by the data, and they are particularly likely in the 2.5–4.5 μm range for the linear (u_1) coefficient of the quadratic law, which is where the retrieved limb-darkening coefficients deviate the most from the theoretical model predictions.

Robustness against eccentricity. We repeated a similar experiment to the ones described above, but this time we set as an input batman model an eccentric orbit with parameters consistent at 3σ with the best-fit parameters presented in ref. 24, corresponding to an eccentricity and argument of periastron of $e = 0.035$ and $\omega = 10°$. Our simulations, presented in Extended Data Fig. 3d, show that these set of values can indeed give rise to offsets between the morning and evening limbs, making the morning limb spectra larger than the evening limb spectra. We explored the range of (e, ω) allowed by the analysis presented in ref. 24 and found that the impact of these parameters always acted in the same direction to the WASP-39 b transit observations analysed in this work, with the values of e and ω allowed by the posterior distribution all potentially giving rise to larger morning depths than evening depths. With the morning and evening spectra reported in this work, we observed the opposite, however—larger evening depths than morning depths. This suggests that the absolute difference we observed between the morning and evening spectra in the NIRSpec/PRISM observations are, at worst, lower limits on the actual absolute depth difference between the morning and the evening limbs.

It is important to note, however, that a set of values of (e, ω) similar to the one used in our experiment would probably be unrealistically large, as secondary eclipse observations constrain $e \cos \omega = 0.0007 \pm 0.0017$ (ref. 49), which would reject such an (e, ω) combination at more than 10σ. Given WASP-39 b's eccentricity is consistent with zero, given data from different sources, which is, in turn, consistent with the relatively small circularization timescales for the planet, WASP-39 being an approximately 9-Ga star[50], we suggest eccentricity offsets are a relatively minor effect for this system.

To test how the most up-to-date constraints on the properties of the system impacted our detection of the morning and evening differences in the transmission spectrum of WASP-39 b presented in this work, we re-ran a white-light light-curve fit similar to that in ref. 24, but assuming an eccentric orbit, and then let the posteriors of the transit parameters of this fit float as priors on our wavelength-dependant light-curve fits, instead of fixing those parameters, as was done in our nominal analysis. This new white-light light-curve fit was performed with two extra priors: (1) the constraint on $e \cos \omega = 0.0007 \pm 0.0017$ of ref. 49; and (2) a prior on the stellar density of WASP-39 b, obtained via the methodology outlined in refs. 51,52. This latter methodology first obtains stellar atmospheric parameters from high-resolution spectra, for which we used an average of three publicly available fibre-fed, extended range echelle spectrograph (FEROS) high-resolution spectra from PID 098.A-9007(A), obtained on 12 February 2017, which were reduced using the CERES pipeline[53]. This spectrum was given as input to the Zonal Atmospheric Stellar Parameters Estimator (ZASPE) code[54], with which an initial set of stellar atmospheric parameters was obtained. Then, the available Gaia ($G = 11.8867 \pm 0.0020$, $B_p = 12.3061 \pm 0.0054$, $R_p = 11.3258 \pm 0.0031$) and Two Micron All Sky Survey (2MASS) ($J = 10.663 \pm 0.024$, $H = 10.307 \pm 0.023$, $K = 10.202 \pm 0.023$) photometry was combined with Gaia-derived distances (211.46 ± 2.35 pc, obtained via parallaxes using the methodology described in ref. 55) to obtain fundamental absolute stellar parameters using PARSEC isochrones[56], with the spectroscopically derived stellar atmospheric parameters used as priors. This iterative procedure returns all the fundamental stellar parameters for the star. In particular, for WASP-39 b, we found $R_* = 0.897 \pm 0.011\, R_\odot$ and $M_* = 0.891 \pm 0.033\, M_\odot$, which, in turn, gave a stellar density of $\rho_* = 1{,}736 \pm 121$ kg m^{-3}. We noted that those estimated stellar parameters were consistent with, and more precise than, those presented in the discovery paper of ref. 50.

This new white-light light-curve fit gives posterior parameters that are, in turn, all consistent with the ones reported in ref. 24, notably, with a stellar density posterior of $1{,}705 \pm 28$ kg m^{-3}, consistent at 1σ with the value of $1{,}699 \pm 55$ kg m^{-3} shown in that work (and much more constrained than our stellar density prior, showcasing this value as not dominated by it). The fit also put a limit on the eccentricity of WASP-39 b of $e < 0.016$ with 99% credibility ($e\sin(\omega) = 0.0014^{+0.0051}_{-0.0057}$; $e\cos(\omega) = 0.0009^{+0.0014}_{-0.0012}$), a circular model still being preferred via the Bayesian evidence. As described above, we then used the posterior distributions of all the transit parameters of this eccentric model fit as priors for each wavelength-dependant light-curve fit using the catwoman NE methodology described above. We found a morning and evening transmission spectrum that is very similar to the one presented in Fig. 2, albeit with larger error bars—an increase dominated by the uncertainty on the eccentricity. This highlights the importance of having high-precision orbital parameters for systems when performing limb asymmetry detections and, in particular, good constraints on eccentricities and arguments of periastron. Despite these enlarged error bars, we still found an average evening-to-morning depth difference of 582 ± 188 ppm—a 3σ detection of the evening-to-morning depth effect presented in this work, even in this worst-case scenario. To further explore the impact of our orbital parameter estimation on our detection of inhomogeneous terminators on WASP-39 b, we ran experiments in which we artificially enlarged the error bars on the orbital parameters by 3-, 5- and 10-fold, for both circular (that is, $e = 0$) and eccentric (that is, free $e \cos(\omega)$ and $e \sin(\omega)$) cases, and compared the average evening-to-morning depths for each case. We compared these differences both across the entire wavelength range and for wavelengths above 4 μm, where we saw the largest deviations in evening-to-morning depths. The results from our experiment are presented in Extended Data Fig. 2. As can be seen, for our circular case, error inflations of up to five times our reported error bars still support our detection of inhomogeneous terminators, whereas for the eccentric case, error inflations of up to three times only support this detection at wavelengths above 4 μm. These experiments highlight the dependency of the detection of this effect on the accuracy and precision of orbital parameters for WASP-39 b, which might also be the case for detecting the effect on other exoplanets. We noted, however, that these experiments provided an upper limit on the uncertainty on the evening-to-morning depth difference because the eccentricity should be wavelength-independent. In our case, however, we were fitting for eccentricity independently for each individual wavelength bin.

Robustness against white-light limb asymmetries. The white-light light-curve analyses performed in ref. 24 assumed a batman transit light-curve model. We left the transit parameters fixed in most of our wavelength-dependent light-curve fits to the NIRSpec/PRISM data. However, given our detection of limb asymmetries in this dataset, it could be that the posterior parameters in ref. 24 are biased, given no catwoman models were used to analyse the JWST data. We performed such fits leaving all the priors for the rest of the parameters unchanged and as described in ref. 24, but allowing for the JWST data to have asymmetric limbs through a catwoman model. We found all the transit parameters agreed within 1σ with respect to the values reported in ref. 24. However, the uncertainties in the time-of-transit centre, eccentricity and stellar density were larger by factors of approximately 1.5, 2 and 4 for the catwoman fits. When accounting for the constraints imposed by WASP-39 b's secondary eclipse, described in the previous paragraph, however, all uncertainties but that of the stellar density were consistent between the analyses. This analysis suggests that the fact that ref. 24 did not use catwoman models to fit the JWST transit light curves is not a particularly important consideration in the case of WASP-39 b, in particular when referring to the constraints on the eccentricity and time-of-transit centre used in our wavelength-dependent fits.

Robustness of morning and evening spectra to planetary rotation. The framework and results presented above omit any impacts from planetary rotation during transit. If this were to be significant, the spectra observed at the very beginning of the transit event could be different from the spectra observed at the end. Assuming the exoplanet is tidally locked, the amount of rotation the planet undergoes (period of around 4.1 days) on timescales of the transit event (approximately 2.8 h) is on the order of approximately 10°, and calculations by Wardenier et al.[57] suggest this might be too small for the detection of any signatures due to planetary rotation. To explore these constraints on our data, we performed the same light-curve analysis outlined above, but considering a different set of morning and evening depths during ingress rather than during egress. We found that during ingress, the mean morning-to-evening transit depth difference was -228 ± 187 ppm, and during egress, the difference was 344 ± 189 ppm. Both values are consistent with zero at 2σ, and thus we were unable to detect any differences between the morning and evening spectra during ingress and egress. We then joined those morning and evening depths, observed during ingress and egress, into a single total transit depth. When comparing the total transit depth during ingress to that of egress, we found a mean difference of 234 ± 144 ppm. This suggests that, while it is possible rotation effects are indeed important, they remain hard to detect with the quality of data at hand.

Robustness of morning and evening spectra to stellar rotation. Stellar rotation could, in principle, produce asymmetries in the transit light curves as the planet transits red- and blue-shifted regions of the star.

WASP-39 b, however, has a very slow stellar rotation of 1.5 ± 0.6 km s^{-1} (ref. 50). In addition, JWST's NIRSpec/PRISM's resolution of about $R = 100$ suggests that such an effect should be small in the case of our observations. We performed calculations to determine how big such an effect would be on our observations and concluded that it would be below 1 ppm, even in the worst-case scenario of a stellar rotation speed at the 5σ limit imposed by the work of Faedi et al.[50]—that is, 4.5 km s^{-1}.

Robustness of morning and evening spectra to stellar heterogeneities. Stellar heterogeneities (caused by, for example, spots and faculae) could, in principle, impact our ability to retrieve limb asymmetries from transit light curves. WASP-39, however, is a relatively quiet G-type star[50]. While photometric variability has been detected in Transiting Exoplanet Survey Satellite and Next Generation Transit Survey light curves with a low amplitude level of 0.06% in ref. 22—on the lower tail of the photometric variability observed in Kepler for G8-type stars like WASP-39 (ref. 58)—no evidence of spot-crossing events on the transit light curves of WASP-39 has been detected so far.

Unnoculted stellar heterogeneities, such as those modelled by the transit light-source effect[58], would impact the limb spectra of the morning and evening in similar ways, and would thus be unable to give rise to the morning and evening differences observed in this work. Occulted cool or hot spots could, in principle, cause asymmetries in the transit light curve. These would, however, have to be larger than about 100 ppm in amplitude in the transit light curve at about 4 μm to give rise to the approximately 400 ppm differences we observed between the mornings and evenings (Fig. 1d). In turn, these should increase in amplitude for shorter wavelengths, which does not match the wavelength-dependence of the limb asymmetries observed in our work. In addition, any such features would be several times larger at optical wavelengths. However, although such features should be easily detectable, no such features were reported in the optical NIRSpec/PRISM light curves analysed in ref. 10.

Based on this, we suggest that stellar activity is unlikely to give rise to the morning and evening differences observed in this work.

Forward models and retrievals

ATMO model grid. We fitted the entire ATMO local condensation grid tailored to WASP-39 b, as introduced in ref. 28. These models included all the dominant species observed in the NIRSpec/PRISM spectrum of WASP-39 b, except for the sulfur species, which were marginally detected in this dataset[10]. To fit the morning and evening spectra, we took into consideration the fact that both are highly correlated, and thus used the log-likelihood framework introduced in ref. 26. To construct the morning and evening depth models, we simply took half the transit depth of a given ATMO model sampled for either the morning or evening limb spectra. Then, we tried all combinations of the models in the grid to fit the morning and evening limb depths. Given that there were 3,920 individual models for WASP-39 b in this grid, this resulted in over 15 million fits.

To bring those models to the observed transit depths in our data, we anchored the mean transit depth of both models to the average evening limb transit depth. This conserved any morning-to-evening transit depth offsets. This offset is, thus, the only free parameter in our model fits. Our set of best-fit models are all consistent with models on which the evening spectrum is hotter by about 200 K than the morning spectrum, spanning a wide range of possible cloud and haze properties. In terms of C/O ratios and metallicities, our best-fit models all produced similar C/O ratios for the morning and evening spectra in the range 0.3–0.6 and metallicities on the order of approximately 10× solar.

CHIMERA atmospheric retrievals. To perform a posterior exploration of the parameter space allowed by our observed morning and evening spectra, we decided to run atmospheric retrievals using the CHIMERA retrieval framework described in ref. 29 and modified in ref. 26 to handle morning and evening spectra. These models include all the dominant species observed in the NIRSpec/PRISM spectrum of WASP-39 b, except for the sulfur species, which were marginally detected in this dataset[10]. This framework performs chemically consistent modelling—that is, it performs chemical equilibrium calculations given the C/O ratios, metallicities and temperature/pressure profiles, which are combined with a prescription for clouds following the work of ref. 59. We used the same prior distributions introduced in ref. 26, the only modification being the prior on the temperature of the limbs, which we set to be a uniform prior of between 500 and 2,000 K for both the morning and evening limbs. Our atmospheric retrievals considered a common metallicity, fiducial 10-bar radius and parameters defining the temperature/pressure profile for the morning and the evening limbs, but considered different C/O ratios, vertical mixing and cloud-top properties for the morning and evening limbs.

The posterior distributions from our CHIMERA atmospheric retrievals—for which a set of posterior parameters are shown in Extended Data Fig. 5—constrained an evening temperature of 1068^{+43}_{-55} K and a morning temperature of 889^{+54}_{-65} K, implying an evening-to-morning difference of 177^{+65}_{-57} K—a 3σ difference between the evening and morning limb temperatures, consistent with the findings from our ATMO best-fit grid model search described above. The rest of the parameters in our atmospheric retrievals were all consistent between the morning and evening limbs, suggesting that this temperature difference is one of the largest effects defining the difference between the morning and evening spectra. In particular, the C/O ratios were consistent with each other, with the evening limb having C/O = $0.58^{+0.13}_{-0.16}$ and the morning limb having C/O = $0.57^{+0.17}_{-0.23}$. Interestingly, while both limbs allowed for clouds, the cloud-top pressure in the evening limb was much more constrained than the pressure in the morning limb, the cloud-top pressure of the evening limb being located in our retrievals at approximately 1–10 mbar and the clouds in the morning limb being consistent with a wide range of possibilities. Notably, the posterior distributions presented in Extended Data Fig. 5 showcase how these cloud properties do not strongly define the morning and evening temperatures, probably stemming from the fact that these two properties are extracted both from the absolute depth difference between the morning and evening spectra and the amplitude of the H_2O and CO_2 features. For example, while the morning cloud-top pressure is consistent with a wide range of values, all those values are allowed within the relatively narrow temperature ranges for the morning and evening temperatures described above. In the case of the evening cloud-top pressure, which is much better defined, some slight correlations are observed with the temperatures, but again within well-constrained temperature values. Finally, the retrieved metallicity in our fits is consistent with a 10× solar metallicity—again, consistent with our best-fit ATMO models.

General circulation models

Condensate cloud model. The results from the cloud-microphysics model presented here were obtained by applying a kinetic cloud-formation model (consistent solution of nucleation of different species, growth and evaporation of mixed materials, gravitational settling, mixing, element conservation), coupled with the equilibrium gas-phase chemistry[60,61] for 10× solar elemental abundances. We used one-dimensional (1D) pressure–temperature profiles as input, extracted from a cloud-free GCM simulation of WASP-39 b using ExpeRT/MITgcm[62]. The mixing timescale in the model was calculated based on the local vertical velocities from the GCM and scale height (see ref. 33). The mixing timescale was then multiplied by a factor of 100 (refs. 63,64). We noted that the GCM simulations were identical to those presented in ref. 32. The resulting cloud particle number densities, their mixed material compositions and mean particle sizes were used as input to calculate the local cloud opacity using the adapted version of petitRADTRANS[65–67], employing the Landau, Lifshitz and Looyenga[68,69] mixing prescription and Mie theory, using the publicly

available Python code PyMieScatt[70]. The spectra from nine different latitudes (−86°, −68°, −45°, −23°, 0°, 23°, 45°, 68°, 86°) were then averaged at the evening and morning terminators, respectively.

Photochemical haze model. For modelling photochemical hazes, we used the haze model presented in ref. 35 in combination with SPARC/MITgcm[71,72], which couples wavelength-dependent radiative transfer using the correlated-k method to a dynamical core based on primitive equations[73]. All numerical choices in the model are identical to the wavelength-dependent passive model presented in ref. 74, except that the planet parameters of WASP-39 b, a 10× solar metallicity and a temperature of the bottom-most layer of 4,154 K were assumed. The model treats hazes as passive tracers with constant particle sizes. Hazes are produced at low pressures on the dayside and destroyed at pressures greater than 0.1 bar. Particle sizes ranging from 1 to 1,000 nm were considered. The haze production rate then was adjusted to obtain a good match to the total (not terminator-resolved) transit spectrum. Particle sizes of 3 and 30 nm resulted in the best match to the transit spectrum. The spectrum shown in Fig. 3 uses a particle size of 30 nm and a haze production rate of 2.5×10^{-12} kg m^{-2} s^{-1} at the substellar point. The spectra generated with a particle size of 3 nm showed qualitatively similar, but smaller, differences between the morning and evening terminators.

Clear-atmosphere equilibrium and transport-induced disequilibrium chemistry models. To model the equilibrium and disequilibrium chemistry (in particular, the transport-induced quenching that occurs when chemical kinetics are coupled to atmospheric transport), WASP-39 b was simulated using the Met Office's Unified Model[75,76]. This model's dynamical core solves the non-hydrostatic, deep-atmosphere Navier–Stokes equations. Its radiative transfer code[77–79] solves the two-stream equations using the correlated-k and equivalent extinction methods, including H_2O, CO, CO_2, CH_4, NH_3, HCN, Li, Na, K, Rb and Cs and collision-induced absorption due to H_2–H_2 and H_2–He as sources of opacity, assuming clear-sky conditions and a 10× solar metallicity. Two different chemistry schemes were used. One was the chemical equilibrium scheme that computes a local chemical equilibrium using the Gibbs energy minimization, and the other was the chemical kinetics scheme that solves the ordinary differential equations describing the evolution of chemical species present in the reduced chemical network of ref. 80 to represent the disequilibrium thermochemistry (in the absence of photolysis), as implemented in refs. 34,81. To maintain stability, the model employs a vertical sponge, with a damping coefficient of 0.15 and a diffusion filter in the longitudinal direction with a coefficient of 3.83×10^{-2} (ref. 76).

Calculating morning and evening spectra. For the photochemical haze and clear-atmosphere models, we generated transmission spectra of WASP-39 b for the morning and evening terminators similarly to the method described in ref. 82. Briefly, we performed absorption-only, ray-striking radiative transfer through the input GCM at two orbital phases. We rotated the GCM by the phase angle at ingress and egress, respectively, in addition to interpolating the GCM onto an equal-altitude grid truncated at approximately 1 bar. For the Met Office's Unified Model, chemical abundances were taken from the GCM output. For the SPARC/MITgcm photochemical haze model, the chemistry was interpolated from the FastChem[83,84] equilibrium chemistry tables.

Our opacity sources included H_2O (ref. 85), CH_4 (refs. 86,87), CO (refs. 88,89), CO_2 (ref. 90), C_2H_2 (ref. 91) and NH_3 (refs. 92,93). We included the extinction (absorption and scattering out of the beam) from haze particles with Mie theory using PyMieScatt[70], assuming homogeneous particles with their size set by the GCM input and a refractive index of soot[94].

A note on 1D versus 3D transit-spectra calculations. We point out that spectra for the condensate cloud model were calculated using a 1D radiative transfer code with the classic mid-transit geometry due to the 1D nature of the microphysics model and the additional complexity of mixed-composition grains. By contrast, the spectra for the photochemical haze model and clear-atmosphere equilibrium and disequilibrium chemistry models were calculated using a 3D code that also correctly takes into account the change in geometry during ingress and egress through rotation. We noted that, in tests comparing the 1D and 3D geometries based on the model grid of ref. 95, the amplitude of the terminator differences changed. In some, but not all, cases, this led to stronger limb asymmetries if the full 3D geometry was considered (K.A. et al., manuscript in preparation). This could potentially bring the size of the observed differences into better agreement with the observations.

Data availability

The raw data from this study are available as part of the Early Release Science Observations (ERS) via the Space Science Telescope Institute's Mikulski Archive for Space Telescopes (https://archive.stsci.edu/). All the figures in this manuscript, along with the associated data and code to reproduce them, can be found at https://github.com/nespinoza/wasp39-terminators. Reduced data along with prior and posterior distributions for our wavelength-dependent catwoman (NE) light curve fits used to obtain the main results of this work can be found at https://stsci.box.com/s/rx7u56zviu3up2p8p34qh3btwop6lgl6. Reduced data along with prior and posterior distributions for our white-light light-curve fit performed for WASP-39 b and described in the Methods can be found at https://stsci.box.com/s/wet5xmacrk26ughr8y2j8wpyjdsumco1. Both datasets contain human-readable outputs and are packaged to be explored using the juliet software library, which is publicly available at https://github.com/nespinoza/juliet.

Code availability

Light curves were fitted using juliet (https://github.com/nespinoza/juliet), batman (https://github.com/lkreidberg/batman), catwoman (https://github.com/KathrynJones1/catwoman) and Tiberius (https://github.com/JamesKirk11/Tiberius), all of which are publicly available.

37. Rustamkulov, Z., Sing, D. K., Liu, R. & Wang, A. Analysis of a JWST NIRSpec lab time series: characterizing systematics, recovering exoplanet transit spectroscopy, and constraining a noise floor. *Astrophys. J. Lett.* **928**, L7 (2022).
38. Espinoza, N. & Jordán, A. Limb darkening and exoplanets: testing stellar model atmospheres and identifying biases in transit parameters. *Mon. Not. R. Astron. Soc.* **450**, 1879–1899 (2015).
39. Howarth, I. D. On stellar limb darkening and exoplanetary transits. *Mon. Not. R. Astron. Soc.* **418**, 1165–1175 (2011).
40. Bourque, M. et al. The exoplanet characterization toolkit (exoctk). Zenodo https://doi.org/10.5281/zenodo.4556063 (2021).
41. Kipping, D. M. Efficient, uninformative sampling of limb darkening coefficients for two-parameter laws. *Mon. Not. R. Astron. Soc.* **435**, 2152–2160 (2013).
42. Patel, J. A. & Espinoza, N. Empirical limb-darkening coefficients and transit parameters of known exoplanets from TESS. *Astron. J.* **163**, 228 (2022).
43. Kirk, J. et al. Rayleigh scattering in the transmission spectrum of HAT-P-18b. *Mon. Not. R. Astron. Soc.* **468**, 3907–3916 (2017).
44. Kirk, J. et al. ACCESS and LRG-BEASTS: a precise new optical transmission spectrum of the ultrahot Jupiter WASP-103b. *Astron. J.* **162**, 34 (2021).
45. Grant, D. & Wakeford, H. R. Exo-tic/exotic-ld: Exotic-ld v3.0.0 (2022). Zenodo https://doi.org/10.5281/zenodo.7437681 (2022).
46. von Paris, P., Gratier, P., Bordé, P., Leconte, J. & Selsis, F. Inferring asymmetric limb cloudiness on exoplanets from transit light curves. *Astron. Astrophys.* **589**, A52 (2016).
47. Barnes, J. W. Effects of orbital eccentricity on extrasolar planet transit detectability and light curves. *Publ. Astron. Soc. Pac.* **119**, 986–993 (2007).
48. Kipping, D. M. Transiting planets – light-curve analysis for eccentric orbits. *Mon. Not. R. Astron. Soc.* **389**, 1383–1390 (2008).
49. Kammer, J. A. et al. Spitzer secondary eclipse observations of five cool gas giant planets and empirical trends in cool planet emission spectra. *Astrophys. J.* **810**, 118 (2015).
50. Faedi, F. et al. WASP-39b: a highly inflated Saturn-mass planet orbiting a late G-type star. *Astron. Astrophys.* **531**, A40 (2011).
51. Brahm, R. et al. K2-232 b: a transiting warm Saturn on an eccentric P = 11.2 d orbit around a V = 9.9 star. *Mon. Not. R. Astron. Soc.* **477**, 2572–2581 (2018).
52. Brahm, R. et al. K2-161b: a low-density super-Neptune on an eccentric orbit. *Mon. Not. R. Astron. Soc.* **483**, 1970–1979 (2019).
53. Brahm, R., Jordán, A. & Espinoza, N. CERES: a set of automated routines for Echelle spectra. *Publ. Astron. Soc. Pac.* **129**, 034002 (2017).

54. Brahm, R., Jordán, A., Hartman, J. & Bakos, G. ZASPE: a code to measure stellar atmospheric parameters and their covariance from spectra. *Mon. Not. R. Astron. Soc.* **467**, 971–984 (2017).
55. Bailer-Jones, C. A. L. Estimating distances from parallaxes. *Publ. Astron. Soc. Pac.* **127**, 994 (2015).
56. Marigo, P. et al. A new generation of PARSEC-COLIBRI stellar isochrones including the TP-AGB phase. *Astrophys. J.* **835**, 77 (2017).
57. Wardenier, J. P., Parmentier, V. & Lee, E. K. H. All along the line of sight: a closer look at opening angles and absorption regions in the atmospheres of transiting exoplanets. *Mon. Not. R. Astron. Soc.* **510**, 620–629 (2022).
58. Rackham, B. V., Apai, D. & Giampapa, M. S. The transit light source effect. II. The impact of stellar heterogeneity on transmission spectra of planets orbiting broadly Sun-like stars. *Astron. J.* **157**, 96 (2019).
59. Ackerman, A. S. & Marley, M. S. Precipitating condensation clouds in substellar atmospheres. *Astrophys. J.* **556**, 872–884 (2001).
60. Woitke, P. & Helling, C. H. Dust in brown dwarfs. III. Formation and structure of quasi-static cloud layers. *Astron. Astrophys.* **414**, 335–350 (2004).
61. Helling, C. H. & Woitke, P. Dust in brown dwarfs. V. Growth and evaporation of dirty dust grains. *Astron. Astrophys.* **455**, 325–338 (2006).
62. Schneider, A. D. et al. Exploring the deep atmospheres of HD 209458b and WASP-43b using a non-gray general circulation model. *Astron. Astrophys.* **664**, A56 (2022).
63. Parmentier, V., Showman, A. P. & Lian, Y. 3D mixing in hot Jupiters atmospheres. I. Application to the day/night cold trap in HD 209458b. *Astron. Astrophys.* **558**, A91 (2013).
64. Samra, D. et al. Clouds form on the hot Saturn JWST ERO target WASP-96b. *Astron. Astrophys.* **669**, A142 (2023).
65. Mollière, P. et al. petitRADTRANS. A Python radiative transfer package for exoplanet characterization and retrieval. *Astron. Astrophys.* **627**, A67 (2019).
66. Mollière, P. et al. Retrieving scattering clouds and disequilibrium chemistry in the atmosphere of HR 8799e. *Astron. Astrophys.* **640**, A131 (2020).
67. Alei, E. et al. Large interferometer for exoplanets (LIFE). V. Diagnostic potential of a mid-infrared space interferometer for studying Earth analogs. *Astron. Astrophys.* **665**, A106 (2022).
68. Landau, L. D. & Lifshitz, E. M. *Electrodynamics of Continuous Media* 2nd edn, Vol. 8 (Pergamon, 1960).
69. Looyenga, H. Dielectric constants of heterogeneous mixtures. *Physica* **31**, 401–406 (1965).
70. Sumlin, B. J., Heinson, W. R. & Chakrabarty, R. K. Retrieving the aerosol complex refractive index using pymiescatt: a mie computational package with visualization capabilities. *J. Quant. Spectrosc. Ra.* **205**, 127–134 (2018).
71. Showman, A. P. et al. Atmospheric circulation of hot Jupiters: coupled radiative-dynamical general circulation model simulations of HD 189733b and HD 209458b. *Astrophys. J.* **699**, 564–584 (2009).
72. Kataria, T. et al. Three-dimensional atmospheric circulation of hot Jupiters on highly eccentric orbits. *Astrophys. J.* **767**, 76 (2013).
73. Adcroft, A., Campin, J.-M., Hill, C. & Marshall, J. Implementation of an atmosphere ocean general circulation model on the expanded spherical cube. *Mon. Weather Rev.* **132**, 2845 (2004).
74. Steinrueck, M. E. et al. Photochemical hazes dramatically alter temperature structure and atmospheric circulation in 3D simulations of hot Jupiters. *Astrophys. J.* **951**, 117 (2023).
75. Wood, N. et al. An inherently mass-conserving semi-implicit semi-Lagrangian discretization of the deep-atmosphere global non-hydrostatic equations. *Q. J. Roy. Meteor. Soc.* **140**, 1505–1520 (2014).
76. Mayne, N. J. et al. The unified model, a fully-compressible, non-hydrostatic, deep atmosphere global circulation model, applied to hot Jupiters. ENDGame for a HD 209458b test case. *Astron. Astrophys.* **561**, A1 (2014).
77. Edwards, J. M. & Slingo, A. Studies with a flexible new radiation code. I: Choosing a configuration for a large-scale model. *Q. J. Roy. Meteor. Soc.* **122**, 689–719 (1996).
78. Amundsen, D. S. et al. Accuracy tests of radiation schemes used in hot Jupiter global circulation models. *Astron. Astrophys.* **564**, A59 (2014).
79. Amundsen, D. S. et al. The UK Met Office global circulation model with a sophisticated radiation scheme applied to the hot Jupiter HD 209458b. *Astron. Astrophys.* **595**, A36 (2016).
80. Venot, O. et al. Reduced chemical scheme for modelling warm to hot hydrogen-dominated atmospheres. *Astron. Astrophys.* **624**, A58 (2019).
81. Drummond, B. et al. Implications of three-dimensional chemical transport in hot Jupiter atmospheres: results from a consistently coupled chemistry-radiation-hydrodynamics model. *Astron. Astrophys.* **636**, A68 (2020).
82. Savel, A. B. et al. No umbrella needed: confronting the hypothesis of iron rain on WASP-76b with post-processed general circulation models. *Astrophys. J.* **926**, 85 (2022).
83. Stock, J. W., Kitzmann, D., Patzer, A. B. C. & Sedlmayr, E. Fastchem: a computer program for efficient complex chemical equilibrium calculations in the neutral/ionized gas phase with applications to stellar and planetary atmospheres. *Mon. Not. R. Astron. Soc.* **479**, 865–874 (2018).
84. Stock, J. W., Kitzmann, D. & Patzer, A. B. C. Fastchem 2: an improved computer program to determine the gas-phase chemical equilibrium composition for arbitrary element distributions. *Mon. Not. R. Astron. Soc.* **517**, 4070–4080 (2022).
85. Polyansky, O. L. et al. ExoMol molecular line lists XXX: a complete high-accuracy line list for water. *Mon. Not. R. Astron. Soc.* **480**, 2597–2608 (2018).
86. Yurchenko, S. N. & Tennyson, J. ExoMol line lists – IV. The rotation–vibration spectrum of methane up to 1500 K. *Mon. Not. R. Astron. Soc.* **440**, 1649–1661 (2014).
87. Yurchenko, S. N., Amundsen, D. S., Tennyson, J. & Waldmann, I. P. A hybrid line list for CH_4 and hot methane continuum. *Astron. and Astrophys.* **605**, A95 (2017).
88. Li, G. et al. Rovibrational line lists for nine isotopologues of the CO molecule in the $X\,^1\Sigma^+$ ground electronic state. *Astrophys. J. Suppl. S.* **216**, 15 (2015).
89. Somogyi, W., Yurchenko, S. N. & Yachmenev, A. Calculation of electric quadrupole linestrengths for diatomic molecules: application to the H_2, CO, HF, and O_2 molecules. *J. Chem. Phys.* **155**, 214303 (2021).
90. Yurchenko, S., Mellor, T. M., Freedman, R. S. & Tennyson, J. ExoMol line lists – XXXIX. Ro-vibrational molecular line list for CO_2. *Mon. Not. R. Astron. Soc.* **496**, 5282–5291 (2020).
91. Chubb, K. L., Tennyson, J. & Yurchenko, S. N. ExoMol molecular line lists – XXXVII. Spectra of acetylene. *Mon. Not. R. Astron. Soc.* **493**, 1531–1545 (2020).
92. Al Derzi, A. R., Furtenbacher, T., Tennyson, J., Yurchenko, S. N. & Császár, A. G. MARVEL analysis of the measured high-resolution spectra of $^{14}NH_3$. *J. Quant. Spectrosc. Ra.* **161**, 117–130 (2015).
93. Coles, P. A., Yurchenko, S. N. & Tennyson, J. ExoMol molecular line lists XXXV: a rotation–vibration line list for hot ammonia. *Mon. Not. R. Astron. Soc.* **490**, 4638–4647 (2019).
94. Lavvas, P. & Koskinen, T. Aerosol properties of the atmospheres of extrasolar giant planets. *Astrophys. J.* **847**, 32 (2017).
95. Roman, M. T. et al. Clouds in three-dimensional models of hot Jupiters over a wide range of temperatures. I. Thermal structures and broadband phase-curve predictions. *Astrophys. J.* **908**, 101 (2021).

Acknowledgements This work is based on observations made with the NASA/ESA/CSA JWST. The data were obtained from the Mikulski Archive for Space Telescopes at the Space Telescope Science Institute, which is operated by the Association of Universities for Research in Astronomy, Inc., under NASA contract NAS 5-03127 for the JWST. These observations are associated with programme no. 1366. M.E.S. acknowledges support from the 51 Pegasi b Fellowship funded by the Heising–Simons Foundation.

Author contributions N.E. led the main analyses and the writing of the paper. N.E. performed the atmospheric retrievals, which were discussed with R.J.M. and L.W. M.E.S. led the compilation of the GCM forward-modelling effort, and led the writing of the GCM section of the paper. J.K., M.M.M. and Z.R. performed the light-curve fits and provided data analysis expertise and feedback to the project as a whole. M.Z., D.C. and N.M. performed the clear-atmosphere equilibrium and transport-induced disequilibrium chemistry simulations. L.C., D.A.L., D.S. and S.K. performed the cloud forward-model simulations. A.B.S. post-processed the GCMs. M.L.-M., E.M.-R.K., E.R., A.D.S., M.M.M., J.K., M.Z., D.C., L.C., J.B., L.D., S.-M.T., E.P., L.M., B.V.R., A.L.C., N.A., K.M., Z.R., N.C. and V.P. provided comments on the manuscript. E.M.M. and A.L.C. led the compilation and analysis of the detector-level data, and provided expertise on the data reduction and analysis. R.B. performed the analysis to obtain the stellar density for WASP-39 b. All co-authors read and agreed with the conclusions of the manuscript.

Competing interests The authors declare no competing interests.

Additional information

Supplementary information The online version contains supplementary material available at https://doi.org/10.1038/s41586-024-07768-4.

Correspondence and requests for materials should be addressed to Néstor Espinoza.

Peer review information *Nature* thanks Drake Deming and the other, anonymous, reviewer(s) for their contribution to the peer review of this work. Peer reviewer reports are available.

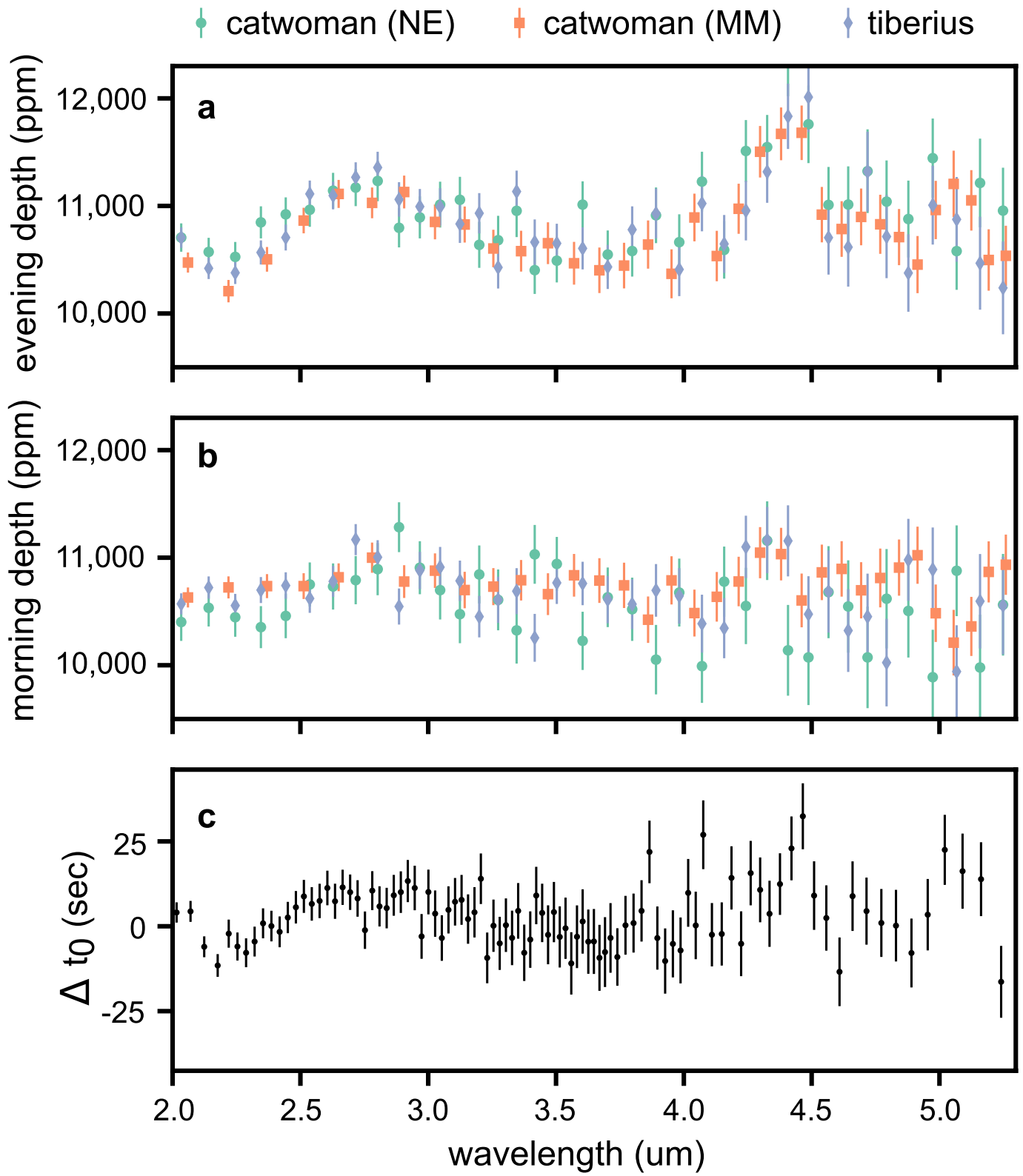

Extended Data Fig. 1 | Different approaches at detecting limb asymmetries from NIRSpec/PRISM data. a-b. Evening (top) and morning (middle) depths as extracted from three independent analyses of our NIRSpec/PRISM lightcurves; one using the catwoman framework with limb-darkening as free parameters with a prior (NE), a framework leaving those fixed (MM) and a framework on which half-ingress and half-egress are fitted independently using a batman lightcurve model (Tiberius); see text for details. Note the agreement between approaches for both terminators, and how the amplitude of the features seem to be smaller in the morning terminator **c**. An independent look at limb asymmetries by fitting for a wavelength-dependent time-of-transit center to each wavelength-dependent lightcurve. As with the top and middle panels, differences between the limbs as tracked by the time-of-transit center seem to be largest between 2–3.5 μm, i.e., around the water bands. All errorbars represent 1-standard deviation.

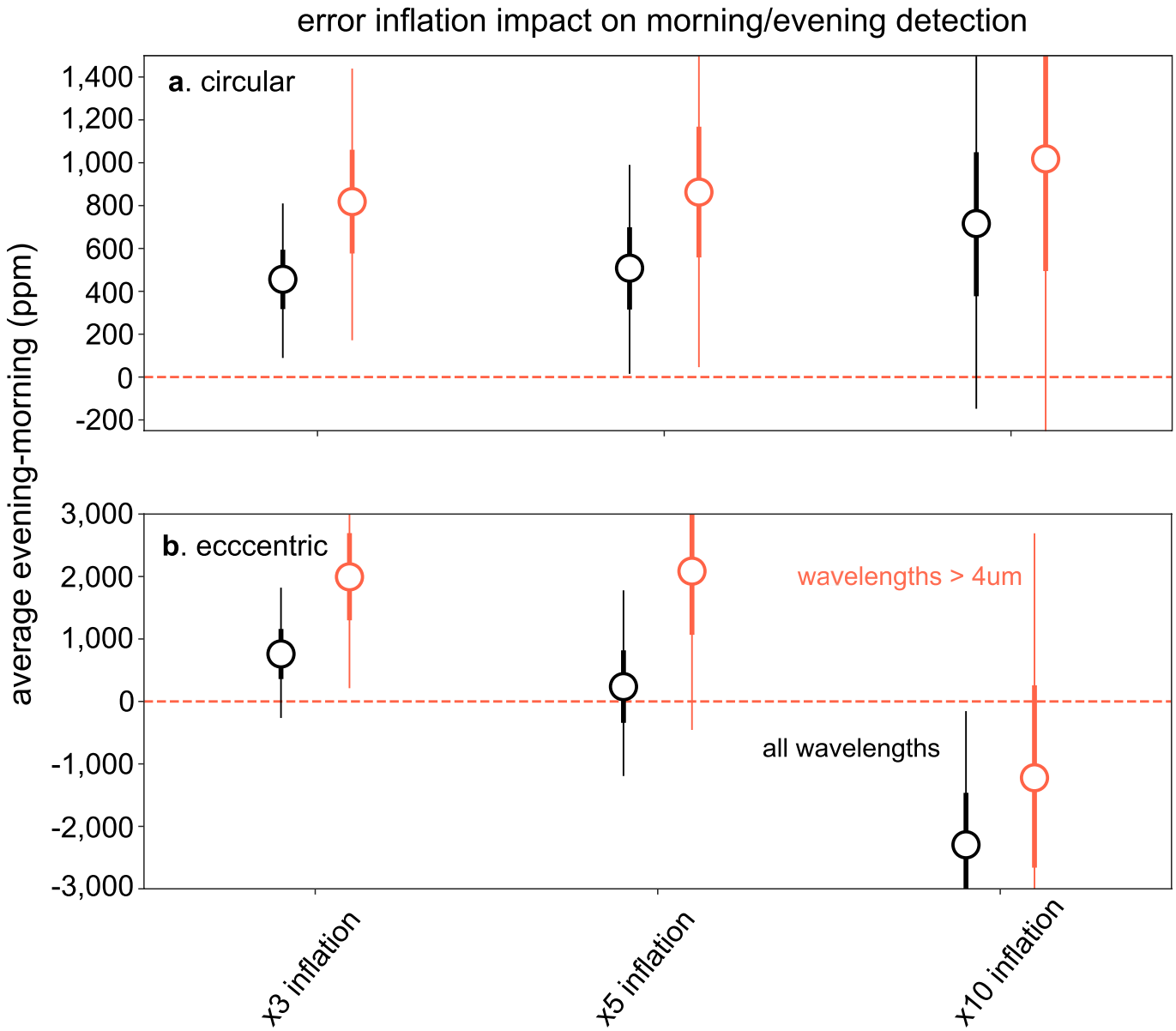

Extended Data Fig. 2 | Impact of less accurate and precise orbital parameters on the detection of inhomogeneous terminators on WASP-39 b. In our experiments, we inflated the errorbars on the orbital parameters (e.g., impact parameter, a/R_*, etc.) by different factors, and performed wavelength-dependant catwoman lightcurve fits on our NIRSpec/PRISM data using normal priors for each parameter along with the other wavelength-dependant parameters described in the main text and in the Methods section such as the planet-to-star radius ratio, limb-darkening, etc. **a.** Error inflation exercise assuming a circular orbit (i.e., eccentricity fixed to zero) and **b.** same exercise but assuming an eccentric orbit – with uncertainties on all parameters, including $e\cos\omega$ and $e\sin\omega$, inflated by 3 (left), 5 (middle) and 10-fold (right). Dashed line marks the non-detection threshold (i.e., equal evening and morning depths). All bold errorbars represent 1-standard deviation. Thin errorbars are 3-standard deviations.

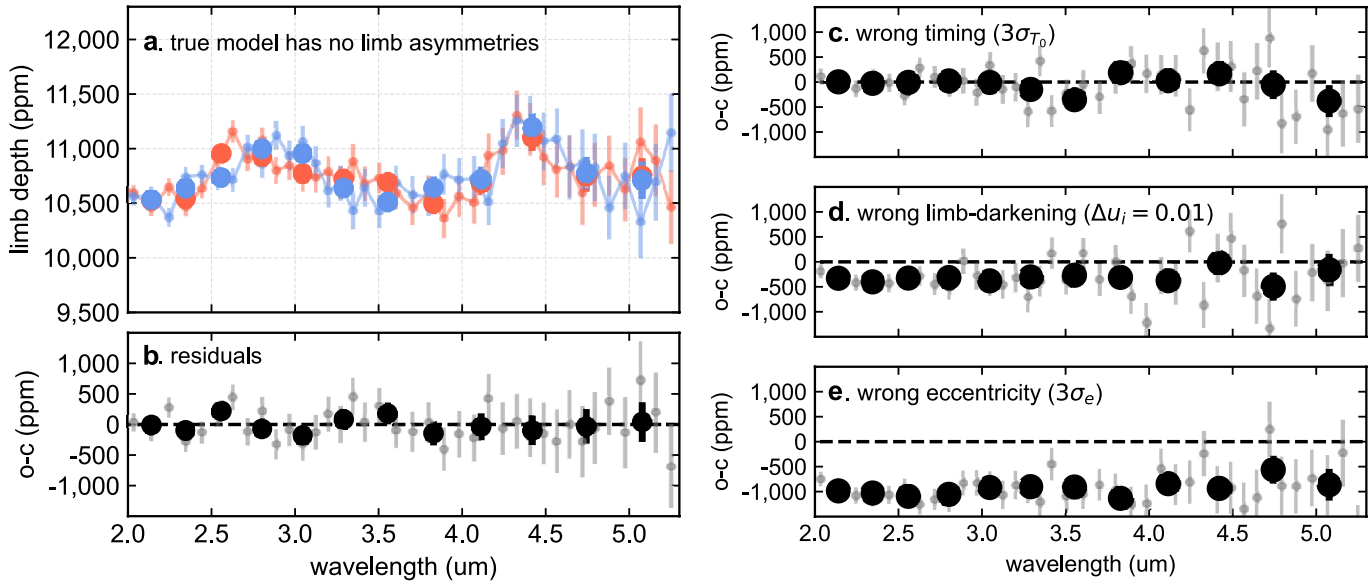

Extended Data Fig. 3 | Robustness of limb asymmetry detection to transit parameters and assumptions. To study the robustness of our extracted morning and evening spectra for the NIRSpec/PRISM observations, we simulated transit lightcurves using batman and then fitted those using catwoman with different assumptions, leaving all parameters fixed but the depths of the morning and evening limbs. **a**-**b**. Null case on which the true model has no limb asymmetries and the input transit parameters are unchanged; the catwoman fits correctly recover the same morning (blue) and evening (red) spectra (top). The difference Δ between the morning and the evening spectra are consistent with zero, as expected from this null case (bottom). **c**. Same experiment as in a., but generating a light curve with a time-of-transit center 3-σ away from the fixed value, which amounts to an offset of 3.4 seconds. The difference Δ is consistent with zero, suggesting our inferences are robust against this parameter. **d**. Same experiment, but generating a light curve that had limb-darkening coefficients of the quadratic law offset by 0.01. Note how this injects a systematic offset in the difference between the morning and evening spectra; depending on the direction of this offset, this can lead to mornings having larger depths than evenings or viceversa. **e**. Same experiment, but generating a transit lightcurve with a non-zero eccentricity consistent at 3-σ with the white-lightcurve fits of Carter & May et al. (in review; $e = 0.035$, $\omega = 10$ deg). Note how this slight eccentricity can generate significantly larger mornings than evenings, due to the asymmetry an eccentric orbit imprints on the transit lightcurve. For WASP-39 b, this eccentricity effect cannot generate larger evenings than mornings, which is what we observe. This suggests our results are also robust against this parameter (see text for details). All errorbars represent 1-standard deviation.

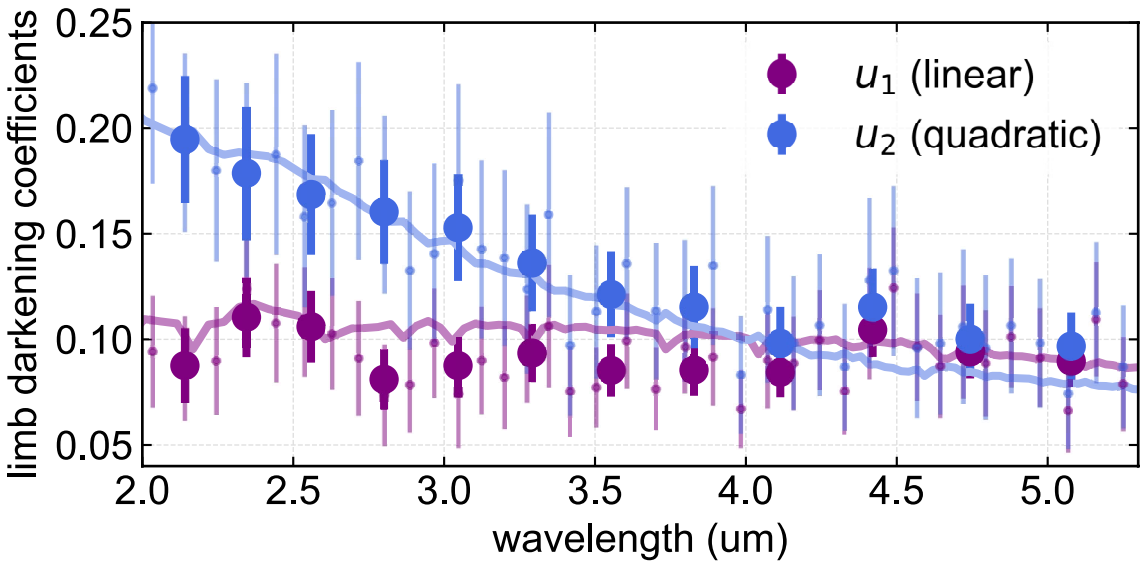

Extended Data Fig. 4 | Quadratic limb-darkening coefficients from catwoman WASP-39 b transit light curve fits. Solid lines (purple for u_1, blue for u_2) are the theoretical limb-darkening coefficients obtained by, first, using the limb-darkening library using ATLAS models to extract limb-darkening coefficients, and then passing those through the SPAM algorithm of[39] to obtain the model predictions. Points with errorbars are retrieved limb-darkening coefficients from our catwoman (NE) transit light curve fits. Note the apparent offset between model and retrieved coefficients between about 2.5 to 4.5 μm for u_1. All errorbars represent 1-standard deviation.

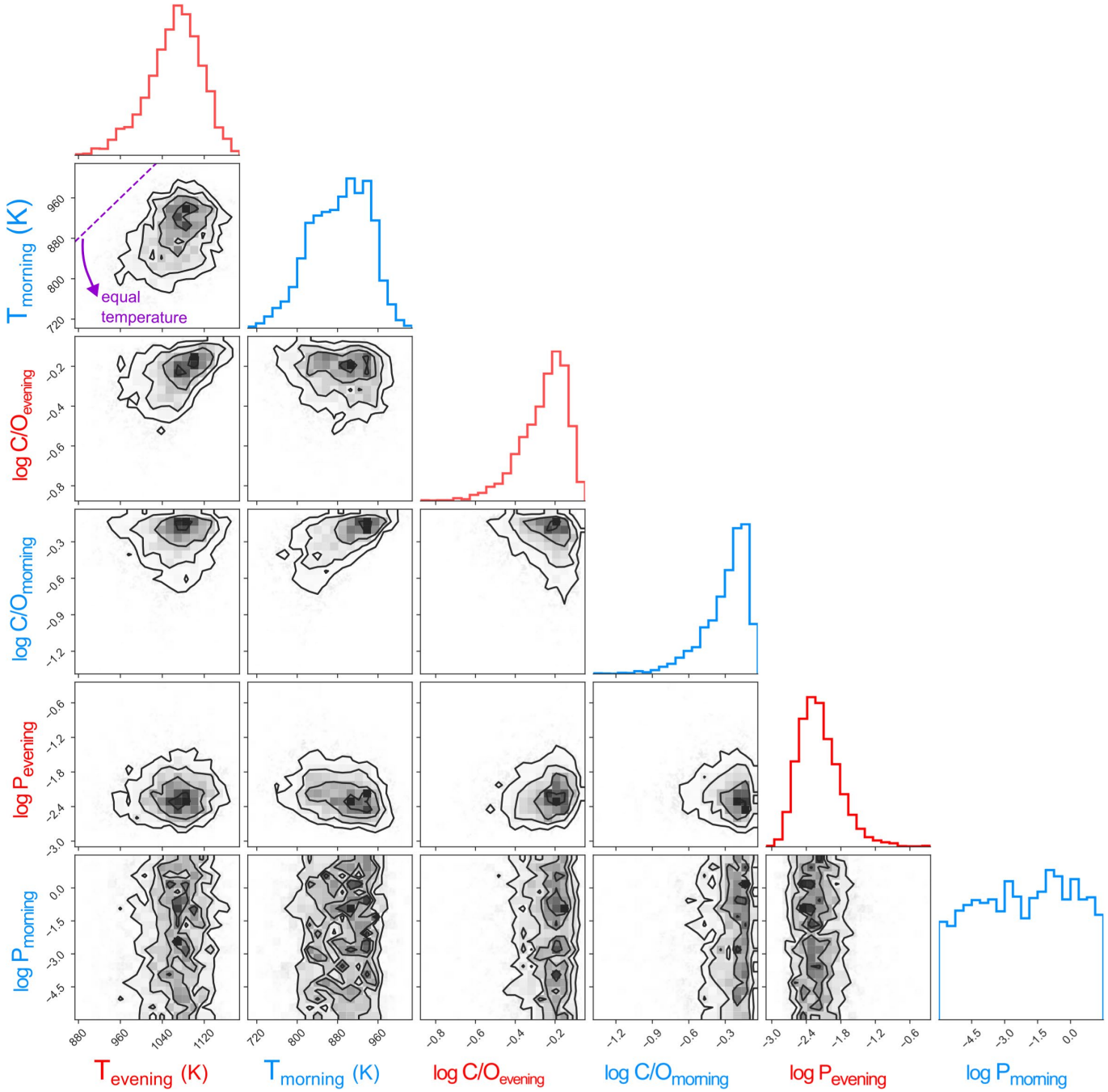

Extended Data Fig. 5 | Posterior distribution of some of the retrieved CHIMERA parameters. Corner plot of the morning/evening temperatures, (log) C/O ratios and (log) cloud-top pressures. Only the evening cloud-top pressure is constrained by our retrievals. The purple line in the morning/evening temperature posterior samples showcases the line of equal temperatures; as can be observed, our posterior samples imply a significantly different morning-to-evening temperature.